

Thamires das Chagas Silva<sup>1</sup> & João Luiz F. Azevedo<sup>2</sup>

<sup>1</sup>Instituto Tecnológico de Aeronáutica, 12228-900, São José dos Campos, SP, Brazil; th.daschagas@gmail.com <sup>2</sup>Instituto de Aeronáutica e Espaço, 12228-904, São José dos Campos, SP, Brazil; joaoluiz.azevedo@gmail.com

#### **Abstract**

This work is part of an ongoing effort to assess the capabilities of nonlinear turbulence models to predict turbulent flows around aeronautical configurations. In the design of complex geometries, the simpler turbulence models tend to have a poor representation of the complex physical phenomena present in the flow around these configurations. In these cases, intending to optimize such aerodynamic shapes, it is necessary to resort to higher fidelity turbulence models, which, in general, are capable of represent more accurately the solution of the flow. Nonlinear eddy-viscosity turbulence models are an intermediate class of turbulence models appropriate to work with the Reynolds-averaged Navier-Stokes (RANS) equations. The main advantage of the nonlinear turbulence models is the capability to predict the flow more accurately at the same time that to keep a computational cost similar to linear eddy-viscosity turbulence models. Two explicit algebraic Reynolds stress models (EARSMs) are employed here, coupled with the 3-D RANS equations. This theoretical formulation is solved by a cell-centered, finite volume method using unstructured meshes. The test cases performed include the transonic flow over the OAT15A airfoil and the subsonic flow over the McDonnell Douglas 30P30N high-lift airfoil.

**Keywords:** CFD, RANS, Nonlinear Turbulence Models, Explicit Algebraic Reynolds Stress Models, Computational Aerodynamics.

## 1. Introduction

Nowadays, computational fluid dynamics (CFD) results have a very significant part in the design phases of an aircraft. This less expensive technique allows optimization of aerodynamic shapes based on the prediction of the flow around the geometries of interest. The accuracy of the results is crucial to achieve this, but, in the context of day-to-day industrial applications, a good balance between accurate results and computational costs is also required.

The Reynolds-averaged Navier-Stokes (RANS) equations are the main formulation used by the industry for aerodynamic simulations. RANS formulation can represent viscous and compressible flows with cost-effective simulations applicable in the industry, and this should remain for many more years [1]. In the RANS formulation, the turbulence effects are brought back into the solution through an appropriate turbulence model. This is made by modeling the Reynolds stress tensor, which appears as the result of the averaging process. The Reynolds stress tensor is a symmetric rank-two tensor of the velocity fluctuations. The more relevant turbulence model classes typically used are the linear eddy-viscosity models (EVMs), the nonlinear eddy-viscosity models (NLEVMs), and the Reynolds stress models (RSMs). They are classified according to the form in which the Reynolds stress tensor is calculated.

The EVMs are the simplest class and also the most used by the industry. It assumes the Boussinesq hypothesis, which states a linear relation between the Reynolds stress tensor and the strain rate tensor of the mean velocity field. This approach presents good results for complex geometries. However, the Boussinesq hypothesis has a significant shortcoming, it does not allow to incorporate

anisotropy in the Reynolds stress tensor. Therefore, in situations in which the anisotropy of the turbulent stresses is relevant, the EVMs results become inaccurate, and may even achieve wrong solutions. Typical situations are boundary layers with an adverse pressure gradient or the interaction between a boundary layer and a shock wave on a transonic wing.

When a higher fidelity representation of the turbulence effects is required in the RANS approach, it is necessary to resort to NLEVMs or RSMs. The last class of models solves one transport equation for each component of the Reynolds stress tensor. Although these models are more advanced turbulence models, the additional computational cost is significant to industry applications. The NLEVMs are an intermediate class of turbulence modeling. This approach allows keeping the structure of a computational code based on EVMs, and incorporating nonlinear terms between the Reynolds stress tensor and the strain rate tensor. Because of that, nonlinear eddy-viscosity turbulence models can present an advantage to incorporating more complex physical effects keeping a computational cost similar to linear eddy-viscosity turbulence models.

Given this background, the present research has the motivation to assess the capabilities of the non-linear eddy-viscosity turbulence models in simulations of turbulent flows for aeronautical applications. In the present work, the main interest is on the study of explicit algebraic Reynolds stress models (EARSMs). An EARSM is formed by a constitutive algebraic model to compute the anisotropy of the Reynolds stresses coupled with an eddy-viscosity model. The constitutive model is obtained by an algebraic expansion of the Reynolds stress tensor as a function of the strain rate tensor and the rotation rate tensor of the mean flow. This expansion relates the Reynolds stress tensor explicitly to the mean flow field through algebraic nonlinear terms, removing the isotropy assumed in the Boussinesq hypothesis. As a result, a nonlinear turbulence model is obtained with a low increase in computational effort compared to EVMs. The present study addresses two EARSMs, labeled here as NLBSL [2] and a modified version of this model, labeled NLBSL-V2 [3]. The EARSMs formulations are described with more details in the Sec. 3.

# 2. Methodology

In this section, the theoretical and numerical formulations used to obtain a numerical solution of the flows of interest in this work are presented. The physical model is presented in the Sec. 2.1. The numerical methods employed to solve the governing equations are presented in the Sec. 2.2.

# 2.1 Physical Model

The flows in the present work are modeled by the Reynolds-averaged Navier-Stokes (RANS) equations, together with appropriate turbulence models to incorporate the effects of turbulence. In Cartesian coordinates, the 3-D RANS equations can be written as [4]

$$\frac{\partial \mathbf{Q}}{\partial t} + \nabla \cdot (\mathbf{P}_e - \mathbf{P}_v) = 0 , \qquad \mathbf{Q} = \begin{bmatrix} \rho & \rho u & \rho v & \rho w & e & \rho \mathcal{T}_1 & \rho \mathcal{T}_2 \end{bmatrix}^T , \qquad (1)$$

where  $\mathbf{Q}$  is the vector of conserved variables,  $\rho$  represents the density of the fluid, u, v and w are the components of the velocity vector,  $\mathbf{v}$ , and e is the total energy per unity of volume. The properties  $\mathcal{T}_1$  and  $\mathcal{T}_2$  represent the turbulent variables, which are defined by the turbulence model. Vectors  $\mathbf{P}_e$  and  $\mathbf{P}_v$  are the inviscid and viscous flux vectors, respectively, determined as

$$\mathbf{P}_{e} = \begin{cases} \mathbf{\rho} \mathbf{v} \\ \mathbf{\rho} u \mathbf{v} + p \hat{\mathbf{i}}_{x} \\ \mathbf{\rho} v \mathbf{v} + p \hat{\mathbf{i}}_{y} \\ \mathbf{\rho} w \mathbf{v} + p \hat{\mathbf{i}}_{z} \\ (e+p) \mathbf{v} \\ \mathbf{\rho} \mathcal{T}_{1} \mathbf{v} \\ \mathbf{\rho} \mathcal{T}_{2} \mathbf{v} \end{cases} , \qquad \mathbf{P}_{v} = \begin{cases} 0 \\ (\tau_{xj} + \tau_{xj}^{t}) \hat{\mathbf{i}}_{j} \\ (\tau_{yj} + \tau_{yj}^{t}) \hat{\mathbf{i}}_{j} \\ (\tau_{zj} + \tau_{zj}^{t}) \hat{\mathbf{i}}_{j} \\ \beta_{j} \hat{\mathbf{i}}_{j} \\ \mu_{diff_{1}} \mathcal{T}_{1,j} \hat{\mathbf{i}}_{j} \\ \mu_{diff_{2}} \mathcal{T}_{2,j} \hat{\mathbf{i}}_{j} \end{cases} . \tag{2}$$

Here, p is the pressure and  $\tau_{ij}$  represents the viscous stress tensor, which is defined as

$$\tau_{ij} = \mu \left[ \left( \frac{\partial u_i}{\partial x_j} + \frac{\partial u_j}{\partial x_i} \right) - \frac{2}{3} \frac{\partial u_m}{\partial x_m} \delta_{ij} \right] , \tag{3}$$

where  $\mu$  is the molecular viscosity coefficient. The variable  $\beta_j$  represents the viscous force work and heat transfer vector, written as  $\beta_j = \tau_{ij}u_i - q_j$ , where  $q_j$  is the heat conduction vector defined as

$$q_{j} = -\gamma \left(\frac{\mu}{Pr} + \frac{\mu_{t}}{Pr_{t}}\right) \frac{\partial \left(e_{i}\right)}{\partial x_{j}} . \tag{4}$$

Here,  $\gamma$  is the specific heat ratio for air,  $e_i$  is the internal energy and Pr and  $Pr_t$  are the Prandtl number and the turbulent Prandtl number, typically assumed to have the values of 0.72 and 0.9, respectively, for aerodynamic applications. The Reynolds stress tensor,  $\tau_{ij}^t$ , and the turbulent viscosity coefficient,  $\mu_t$ , are related to the turbulence model. The modeling of these variables by the turbulence model should be able to include the turbulence effects into the RANS equations. More details about the turbulence models employed in this work are presented in the Sec. 3.

## 2.2 Numerical Methods

The RANS equations are solved in a cell-centered finite volume formulation, written as

$$\frac{\partial \mathbf{Q}_i}{\partial t} = -\frac{1}{V_i} \sum_{k=1}^{nf} \left[ (\mathbf{P}_{e_k} - \mathbf{P}_{v_k}) \cdot \mathbf{S}_k \right] . \tag{5}$$

In Eq. (5), k subscript represents properties computed in the k-th face, and nf is the number of faces of the i-th control volume.  $S_k$  is the area vector of the k-th face. The convective fluxes are discretized by the Roe scheme [5], with the property values obtained in the k-th face by a linear reconstruction of the primitive properties at the control volume faces performed using the MUSCL scheme [6]. In regions with strong gradients in the flow, the linear reconstruction requires a limiter function in order to prevent non-physical oscillations of the solution. The limiter function used in this work is the van Albada limiter function extended for the multidimensional case [7].

For the discretization of the viscous fluxes in the k-th face, the value of  $\mathbf{Q}$  property gradients at the volume faces is necessary. For this, the gradients are computed as cell-averaged gradients by the Green-Gauss theorem [8]. Afterwards, the property gradients are extrapolated to the volume faces by the scheme [8–10]

$$(\nabla \phi)_k = (\nabla \phi)_{V00} - \left[ (\nabla \phi)_{V00} \cdot \frac{\vec{r}_k}{|\vec{r}_k|} - \frac{\phi_j - \phi_i}{|\vec{r}_k|} \right] \frac{\vec{r}_k}{|\vec{r}_k|} , \qquad (\nabla \phi)_{V00} = \frac{1}{V_i + V_j} (V_i \nabla \phi_i + V_j \nabla \phi_j) .$$
 (6)

Here, the i and j subscripts represent the cell to the left and the cell to the right of the k-th face, respectively, and  $\vec{r}_k$  is the distance between the cell centroids that share the same k-th face.  $\phi$  is a property of the vector of conserved variables,  $\mathbf{Q}$ , and V is the volume of the cell. The time march is performed by an implicit Euler scheme [4] and the linear system is solved by a symmetric Gauss-Seidel iterative method.

# 3. Explicit Algebraic Reynolds Stress Models

The two EARSMs addressed in this work use the constitutive algebraic model derived by Wallin and Johansson [11], which is presented in Sec. 3.1. This constitutive model is integrated with the eddy-viscosity model calibrated by Hellsten [2], discussed in the Sec. 3.2. The resulting model is referred here as NLBSL. The second EARSM used in this work, called NLBSL-V2, is also discussed in Sec. 3.2.

# 3.1 The Constitutive Algebraic Model

Firstly, the Reynolds stress tensor is divided into an isotropic part and anisotropic part, written as

$$\tau_{ij}^{t} = 2C_{\mu}^{eff} \rho k \tau S_{ij} - \frac{2}{3} \rho k \delta_{ij} - \rho k a_{ij}^{(ex)} , \qquad (7)$$

where  $\tau$  is a characteristic time of the turbulence,  $S_{ij}$  is the strain rate tensor, and  $a_{ij}^{(ex)}$  is the extra anisotropy tensor. The constitutive model defines the effective coefficient,  $C_{\mu}^{eff}$ , so the eddy-viscosity model determines the isotropic part. The anisotropic tensor is fully determined by the constitutive model as a function of the strain rate tensor and of the rotation rate tensor,  $S_{ij}$  and  $\Omega_{ij}$ , respectively. The most general form for the anisotropic tensor consists of ten tensorially independent groups [11], in which all higher-order tensor combinations can be reduced with the aid of the Caley-Hamilton theorem to

$$\mathbf{a} = \beta_{1}\tilde{\mathbf{S}} + \beta_{2}\left(\tilde{\mathbf{S}}^{2} - \frac{1}{3}II_{S}\mathbf{I}\right) + \beta_{3}\left(\tilde{\mathbf{\Omega}}^{2} - \frac{1}{3}II_{\Omega}\mathbf{I}\right) + \beta_{4}\left(\tilde{\mathbf{S}}\tilde{\mathbf{\Omega}} - \tilde{\mathbf{\Omega}}\tilde{\mathbf{S}}\right) + \beta_{5}\left(\tilde{\mathbf{S}}^{2}\tilde{\mathbf{\Omega}} - \tilde{\mathbf{\Omega}}\tilde{\mathbf{S}}^{2}\right) + \beta_{6}\left(\tilde{\mathbf{S}}\tilde{\mathbf{\Omega}}^{2} + \tilde{\mathbf{\Omega}}^{2}\tilde{\mathbf{S}} - \frac{2}{3}IV\mathbf{I}\right) + \beta_{7}\left(\tilde{\mathbf{S}}^{2}\tilde{\mathbf{\Omega}}^{2} + \tilde{\mathbf{\Omega}}^{2}\tilde{\mathbf{S}}^{2} - \frac{2}{3}V\mathbf{I}\right) + \beta_{8}\left(\tilde{\mathbf{S}}\tilde{\mathbf{\Omega}}\tilde{\mathbf{S}}^{2} - \tilde{\mathbf{S}}^{2}\tilde{\mathbf{\Omega}}\tilde{\mathbf{S}}\right) + \beta_{9}\left(\tilde{\mathbf{\Omega}}\tilde{\mathbf{S}}\tilde{\mathbf{\Omega}}^{2} - \tilde{\mathbf{\Omega}}^{2}\tilde{\mathbf{S}}\tilde{\mathbf{\Omega}}\right) + \beta_{10}\left(\tilde{\mathbf{\Omega}}\tilde{\mathbf{S}}^{2}\tilde{\mathbf{\Omega}}^{2} - \tilde{\mathbf{\Omega}}^{2}\tilde{\mathbf{S}}^{2}\tilde{\mathbf{\Omega}}\right).$$
(8)

The tensorial notation is used in the Eq. (8), where  $\tilde{\mathbf{S}} = \tau S_{ij}$ ,  $\tilde{\mathbf{\Omega}} = \tau \Omega_{ij}$ , and  $\mathbf{I}$  is the identity tensor. The  $\beta$  coefficients are obtained in terms of the five independent invariants,

$$II_S = \operatorname{tr}\{\tilde{\mathbf{S}}^2\}, \quad II_{\Omega} = \operatorname{tr}\{\tilde{\mathbf{\Omega}}^2\}, \quad III_S = \operatorname{tr}\{\tilde{\mathbf{S}}^3\}, \quad IV = \operatorname{tr}\{\tilde{\mathbf{S}}\tilde{\mathbf{\Omega}}^2\}, \quad V = \operatorname{tr}\{\tilde{\mathbf{S}}^2\tilde{\mathbf{\Omega}}^2\},$$
 (9)

where  $\{\}$  denotes the trace of the tensor. For the 3-D case, the explicit solution obtained by Wallin and Johansson [11] reduced the anisotropy tensor for five tensorially independent groups, which are related to the  $\beta$  coefficients defined as

$$\beta_{1} = -\frac{N(2N^{2} - 7II_{\Omega})}{Q}, \quad \beta_{3} = -\frac{12N^{-1}IV}{Q},$$

$$\beta_{4} = -\frac{2(N^{2} - 2II_{\Omega})}{Q}, \quad \beta_{6} = -\frac{6N}{Q}, \quad \beta_{9} = \frac{6}{Q}, \quad (10)$$

and all others  $\beta$  coefficients are identically null. The expressions for N and Q, considering the 3-D case, can be found in the Refs. [2, 11]. The anisotropic contribution,  $a_{ij}^{(ex)}$ , is given by Eqs. (8) and (10), minus the isotropic part, resulting in

$$\mathbf{a}^{(ex)} = \beta_3 \left( \tilde{\mathbf{\Omega}}^2 - \frac{1}{3} I I_{\Omega} \mathbf{I} \right) + \beta_4 \left( \tilde{\mathbf{S}} \tilde{\mathbf{\Omega}} - \tilde{\mathbf{\Omega}} \tilde{\mathbf{S}} \right)$$

$$+ \beta_6 \left( \tilde{\mathbf{S}} \tilde{\mathbf{\Omega}}^2 + \tilde{\mathbf{\Omega}}^2 \tilde{\mathbf{S}} - I I_{\Omega} \tilde{\mathbf{S}} - \frac{2}{3} I V \mathbf{I} \right) + \beta_9 \left( \tilde{\mathbf{\Omega}} \tilde{\mathbf{S}} \tilde{\mathbf{\Omega}}^2 - \tilde{\mathbf{\Omega}}^2 \tilde{\mathbf{S}} \tilde{\mathbf{\Omega}} \right).$$

$$(11)$$

The effective coefficient present in Eq. (7) is defined by the turbulence model as

$$C_{\mu}^{eff} = -\frac{1}{2} \left( \beta_1 + II_{\Omega} \beta_6 \right) . \tag{12}$$

It is important to note that, now, this coefficient is variable with the solution rather than a constant value as usually used in linear eddy-viscosity turbulence models. Typically, in EVMs of two equations, this constant is set as  $C_{\mu}=0.09$ .

# 3.2 Coupling with the Eddy-Viscosity Model

The constitutive model presented in the previous section is coupled to the eddy-viscosity model calibrated by Hellsten [2]. Together, these formulations result in the nonlinear turbulence model referred to here as the NLBSL model. The EVM calibrated by Hellsten is a two-equation turbulence model that solves one transport equation for k and one transport equation for k, which are written as

$$\frac{\partial(\rho k)}{\partial t} + \frac{\partial(\rho u_{j}k)}{\partial x_{j}} = P_{k} - \beta^{*}\rho\omega k + \frac{\partial}{\partial x_{j}} \left[ (\mu + \sigma_{k}\mu_{t}) \frac{\partial k}{\partial x_{j}} \right],$$

$$\frac{\partial(\rho\omega)}{\partial t} + \frac{\partial(\rho u_{j}\omega)}{\partial x_{j}} = \gamma \frac{\omega}{k} P_{k} - \beta\rho\omega^{2} + \frac{\partial}{\partial x_{j}} \left[ (\mu + \sigma_{\omega}\mu_{t}) \frac{\partial\omega}{\partial x_{j}} \right] + \sigma_{d} \frac{1}{\omega} \max \left( \frac{\partial k}{\partial x_{j}} \frac{\partial\omega}{\partial x_{j}}; 0 \right).$$
(13)

The model computed the production term of k as

$$P_k = \tau_{ij}^t \frac{\partial u_i}{\partial x_j} \,, \tag{14}$$

where  $\tau_{ij}^{\iota}$  is the Reynolds stress tensor, defined by Eq. (7). The constants of the model are calculated by

$$\phi = F_1 \phi_1 + (1 - F_1) \phi_2 , \qquad (15)$$

where  $\phi$  represents any constant of the model and the transfer function,  $F_1$ , is defined as

$$F_1 = \tanh(1.5\arg_1^4)$$
, (16)

$$\arg_{1} = \min \left[ \max \left( \frac{\sqrt{k}}{\beta^* \omega d}; \frac{500 v}{d^2 \omega} \right); \arg_{2} \right], \tag{17}$$

$$\arg_2 = \frac{20k}{\max[d^2(\nabla k \cdot \nabla \omega)/\omega; \ 200k_{\infty}]} \ . \tag{18}$$

In Eq. (13),  $\beta^* = 0.09$ . The turbulent eddy-viscosity coefficient,  $\mu_t$ , is defined as

$$\mu_t = C_\mu^{eff} \rho k \tau \ . \tag{19}$$

This is the NLBSL turbulence model, the model originally calibrated by Hellsten [2] with an interest in high-lift flows. However, many aeronautical applications have compressibility effects due the presence of shock waves in the flow. Therefore, a modification was made in the original NLBSL model in order to make it more sensitive to compressibility effects.

Usually, the  $k-\omega$  turbulence models define the  $\mu_t$  as proportional to  $k/\omega$ . The original NLBSL model multiplies the production term in the  $\omega$  equation, Eq. (13), by  $\omega/k$ . This is equivalent to defining the coefficient  $\mu_t$  as in the BSL model, in which  $\mu_t = \rho k/\omega$ , and then dividing the production term in the  $\omega$  equation by  $\nu_t$ . In the SST model, which is a  $k-\omega$  model, the production term in the  $\omega$  equation is divided directly by the  $\nu_t$  coefficient. Thus this modification is implemented in the original NLBSL formulation, writing the  $\omega$  equation as

$$\frac{\partial(\rho\omega)}{\partial t} + \frac{\partial(\rho u_j\omega)}{\partial x_j} = \gamma \frac{P_k}{v_t} - \beta \rho \omega^2 + \frac{\partial}{\partial x_j} \left[ (\mu + \sigma_\omega \mu_t) \frac{\partial \omega}{\partial x_j} \right] + \sigma_d \frac{1}{\omega} \max \left( \frac{\partial k}{\partial x_j} \frac{\partial \omega}{\partial x_j}; 0 \right). \tag{20}$$

Hence, the unique difference between this equation and the  $\omega$  equation from the original NLBSL turbulence model, Eq. (13), is in the production term. For the  $\omega$  equation written as in Eq. (20), the EARSM is addressed in this work as the NLBSL-V2 model.

## 4. Results

Two test cases concerned about aeronautical applications have been addressed in the present work. The first case is the transonic flow over an OAT15A airfoil and the second case is the high-lift flow over the McDonnell Douglas 30P30N multi-element airfoil. The results are compared with experimental data and, in order to estimate the improvements of the nonlinear turbulence models over linear turbulence models, the results are also compared with a version of the SST turbulence model [12]. This version was previously implemented in the same CFD code used here [13] and it is labeled as the SST-2003 turbulence model [14] in the turbulence modeling resource (TMR) web page of the NASA Langley Research Center. Such studies are presented below.

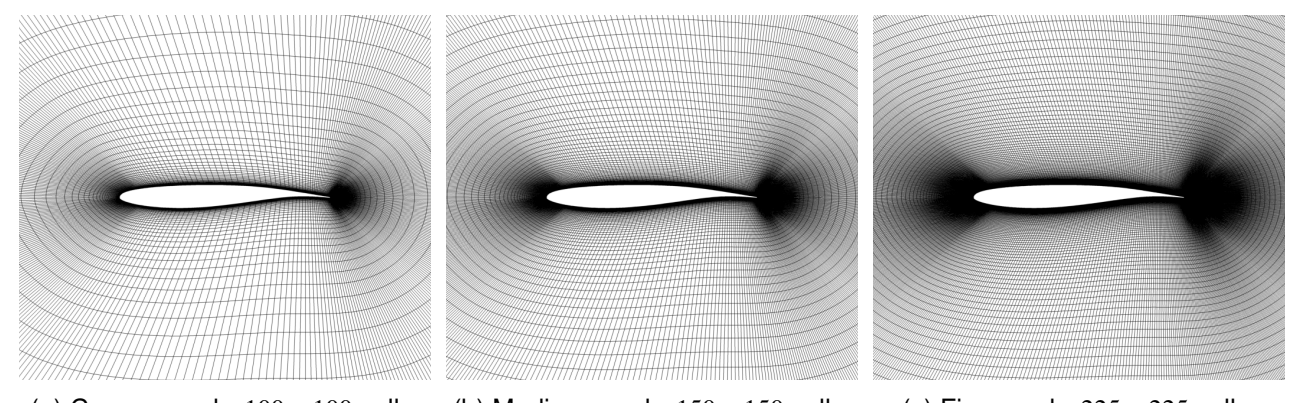
# 4.1 Transonic Flow over OAT15A Airfoil

This case was chosen to investigate the capabilities of the EARSMs addressed here to handle the shock wave on the upper surface of the airfoil and the interaction between this shock and the boundary layer. The objective is to assess how significant the effect of the anisotropy of the turbulent stresses is in this physical problem. The transonic flow over the OAT15A airfoil studied here is described in Ref. [15] as case A-11, whose flow conditions are shown in Tab. 1.

Table 1 – Flow conditions for the OAT15A airfoil case.

$M_{\infty}$	Re	Chord [m]	T [K]	$\alpha$ [deg]
0.724	$3 \times 10^6$	1.0	246.66	1.15

In this study, three hexahedral mesh levels are used with a global refinement factor of 1.5 between each mesh level, and 1.1 growth factor in the wall normal direction. Figure 1 shows the visualization of the meshes. The nomenclature  $100 \times 100$  below the coarse mesh, Fig. 1a, means there are 100 cells both along the airfoil and the normal direction. The same is valid for the other meshes. The CFD code used in this research can only handle with three-dimensional grids. Therefore, the 2-D cases presented here are 2-D geometries with one extruded control volume in the spanwise direction. This is a good practice for these cases because there are no expectations that 3-D effects will be relevant to the solutions. The results for this study case are compared with experimental data [15] and with results from the SST turbulence model [12, 14].



(a) Coarse mesh:  $100 \times 100$  cells. (b) Medium mesh:  $150 \times 150$  cells. (c) Fine mesh:  $225 \times 225$  cells.

Figure 1 – The three meshes used in the studies of the OAT15A airfoil.

In order to ensure the high-quality mesh for capturing the flow using turbulence closures, the three meshes follow the recommended  $y^+$  spacing for the first cell center from the wall. For aeronautical applications, the commonly suggested value of  $y^+$  spacing is  $y^+ \le 1$  over the entire airfoil. This parameters helps to ensure a good resolution of the wall effects in the simulations. Figure 2 shows the  $y^+$  values over the airfoil for the three meshes employed in this test case.

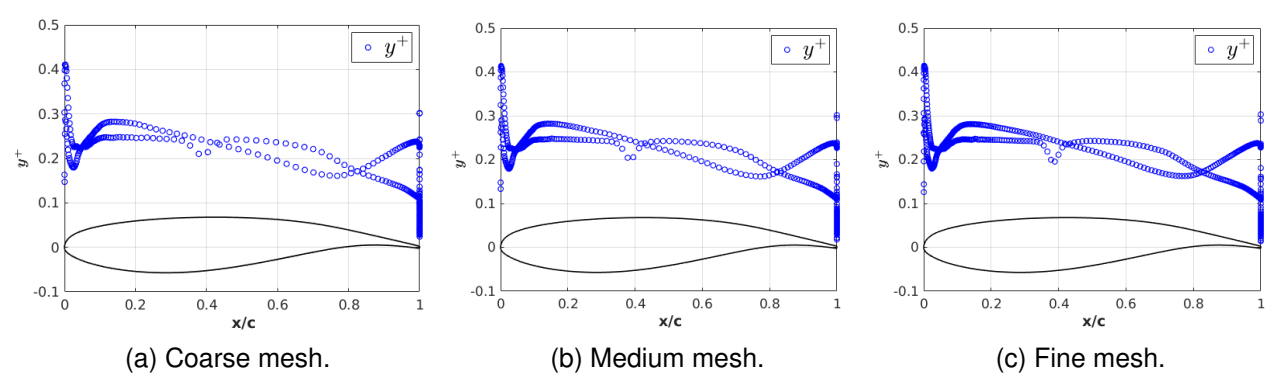


Figure 2 – Values of  $y^+$  over the OAT15A airfoil for the three meshes used in this case.

Tables 2 and 3 show the aerodynamic coefficient values obtained with the two nonlinear turbulence models and the SST turbulence model. Experimental values were extracted by interpolation from plots available in Ref. [15]. For this flow condition, the reference data are approximately  $C_L = 0.5949$  and  $C_D = 0.0106$ .

Table 2 – Lift coefficients ( $C_L$ ) from OAT15A airfoil case and the percentage of the error for each simulation.

Mesh Level	SST	%sst	NLBSL	%NLBSL	NLBSL-V2	%NLBSL-V2
Medium	0.68081 0.68216 0.68329	14.7	0.68257	14.7 14.7 14.9	0.66006 0.66033 0.66122	11.0 11.0 11.1

Table 3 – Drag coefficients ( $C_D$ ) from OAT15A airfoil case and the percentage of the error for each simulation. Values of drag in drag counts.

Mesh Level	SST	%sst	NLBSL	% <sub>NLBSL</sub>	NLBSL-V2	%NLBSL-V2
Coase			129.76	22.4	121.11	14.3
Medium	124.00	17.0	127.79	20.6	118.91	12.2
Fine	122.10	15.2	126.86	19.7	117.87	11.2

Looking at the  $C_L$  results in Tab. 2, one can observe that the percentage error variation with the mesh refinement is minimal using the same turbulence model. However, the NLBSL-V2 results exhibit a lower percentage error compared to the other models. In general, there is a noticeable gap between the computed coefficients and the experimental values. For the  $C_D$  coefficients, Tab. 3, the error percentage is larger for the three turbulence models compared to the error percentage of the  $C_L$  coefficients. Furthermore, the  $C_D$  coefficients are affected more significantly by changes in mesh refinement. However, despite this sensitivity, the variations between consecutive mesh levels for the same turbulence model are lower than 2%. This is valid for the three turbulence closures used.

Such results show that mesh independence has not yet been achieved. Given the purpose of this work, such changes in aerodynamic coefficients are considered very small and, hence, the fine mesh is considered sufficiently refined to continue the investigations of this study case. The disparity between the numerical and experimental values is also attributed to the inherent limitations of each turbulence model in accurately capturing the physical characteristics present in this flow.

It is important to observe from results presented in Tabs. 2 and 3 that each turbulence model seems to converge to different values of the aerodynamic coefficients. This is expected, because, as discussed in Sec. 2.1 the turbulence model is part of the physical formulation. Therefore, for simulations using

different turbulence models, the solutions should be also different from each other.

Figure 3 shows the results of the pressure coefficient distributions over the OAT15A airfoil obtained with the fine mesh. The square drawn in the Fig. 3a highlights the shock wave region, which is displayed in an enlarged view in Fig. 3b. The three turbulence models have the same representation of the pressure coefficients on the lower surface of the airfoil, although there are small differences from the experimental data. On the upper surface, the results among the different turbulence models are very close, except for the shock wave region. As one should expect, none of the turbulence models is able to capture the laminar-turbulent transition that can be observed in the experimental data close to the leading edge, at x/c approximately 0.13, since the simulations are performed considering fully turbulent flow.

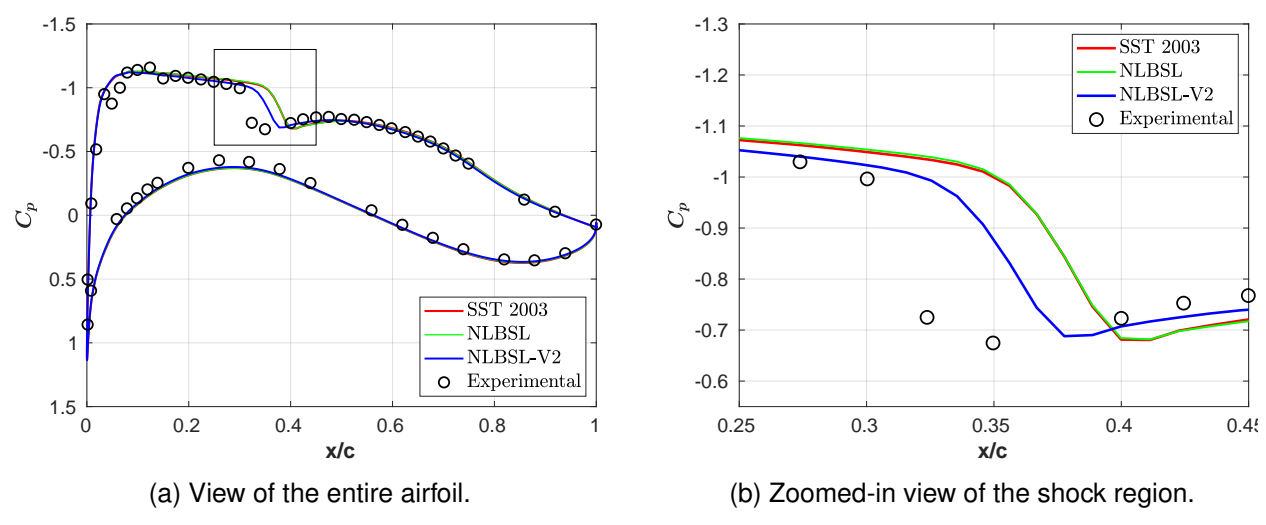


Figure 3 – Pressure coefficient distributions over the OAT15A airfoil.

The solutions of the SST and NLBSL turbulence models, represented by the red and green curves, respectively, are very close to each other over all regions of the airfoil. The NLBSL model was derived from the BSL model, a version of the SST model with a simpler definition of the eddy-viscosity coefficient. Furthermore, the NLBSL model was originally applied to high-lift flows. In such conditions, the compressibility effects are smaller than in a transonic flow. This is an indication of why the NLBSL model, even being a more advanced turbulence model, has a behavior similar to the SST model in this case. During the development of a turbulence model, the model constants are determined through evaluating the model results for a set of test cases, resulting in a model that works very well for cases in which the physical phenomena are similar to those used to calibrate it. Therefore, since the NLBSL model was not originally calibrated for strong compressibility effects, its behavior is, for this case, similar to that provided by the SST turbulence model, which represents the original formulation from which the NLBSL model was developed.

The solution obtained with the NLBSL-V2 turbulence model, the blue curve, is in better agreement with the experimental data, particularly in the shock region. This result seems to indicate that the modification made in the production term of the  $\omega$  equation, from the original NLBSL, becoming the NLBSL-V2 turbulence model, produced a significant improvement in the ability of the model to deal with transonic flows by making it more sensitive to compressibility effects. Thus, the behavior of the NLBSL-V2 model is the result of a more advanced turbulence model, considering an anisotropic formulation together with compressibility effects. However, looking at the results from NLBSL and NLBSL-V2 turbulence models, the compressibility effects are predominant over the anisotropy effects, since NLBSL also has an anisotropic formulation but was not able to capture the shock wave location with more accuracy than the SST model solution.

Given these results, the NLBSL-V2 model is the nonlinear turbulence model more appropriate for this case. A more detailed analysis between the three closures is performed to assess the characteristic of each turbulence model. Figure 4 displays the mean turbulence kinetic energy field,  $\rho k$  [J/m³],

around the airfoil. Three specific regions are identified for a more detailed comparison of the results obtained.

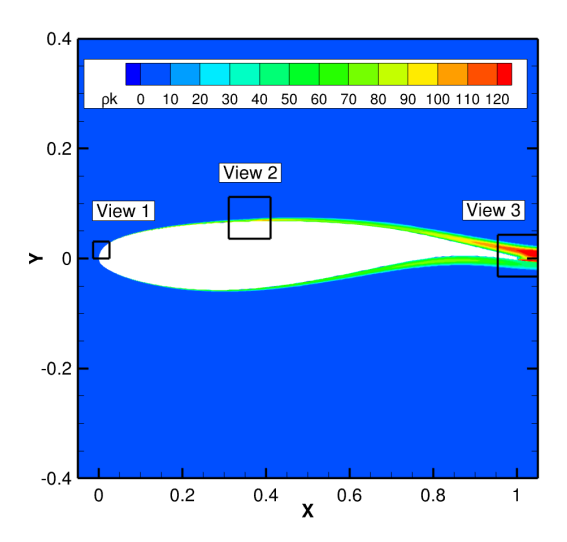


Figure 4 – Field of  $\rho k$  around the OAT15A airfoil. Three specific regions identified for analysis.

Figure 5 shows an enlarged visualization of the view 1 region, which is near the leading edge. It is possible to identify a layer around the airfoil where there is a significant production of mean turbulence kinetic energy. The circles in Figs. 5a and 5c indicate the beginning of the growth of this layer. In the NLBSL solution, Fig. 5b, the beginning of the growth of this layer is beyond the boundaries of the plot. It is important to underline that these regions highlighted by the circles have no relation with the laminar-turbulent transition phenomenon since the simulations are run considering fully turbulent flow. The objective of highlighting these regions is to see how each turbulence model predicts the  $\rho k$  fields and how this affects the solution of the problem. The NLBSL turbulence model computed the beginning of this region further upstream than the SST and NLBSL-V2 model solutions. It is observed that, in this region, the NLBSL model shows a  $\rho k$  layer formed around the airfoil that is slightly more energized compared to the ones computed by the SST and NLBSL-V2 model solutions, as indicated by the yellow area in Fig. 5b, showing that the NLBSL model computes higher levels of  $\rho k$ .

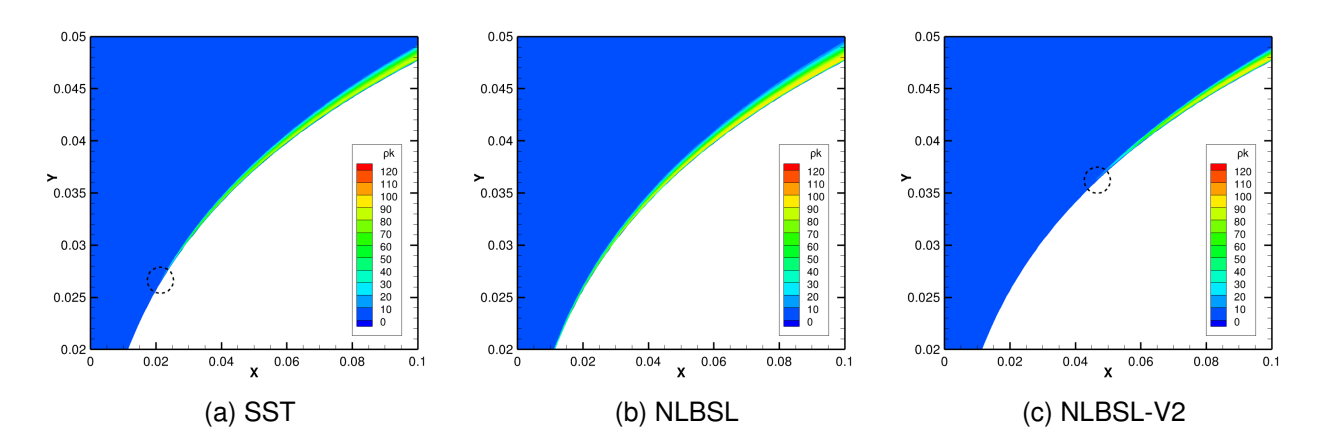


Figure 5 – Results for the  $\rho k$  field around the OAT15A airfoil. View 1 region from Fig. 4.

Figure 6 shows the view 2 region from Fig. 4. The dashed lines indicate the rough location of the shock wave computed by each turbulence model. For the three solutions, one can observe that there is a layer with significant production of mean turbulence kinetic energy immediately downstream the

shock wave. However, in the NLBSL results, there are significantly larger values of  $\rho k$  compared to the other turbulence models. Immediately after the shock wave, the layer with a significant production of mean turbulence kinetic energy is thicker in the NLBSL solution. In the NLBSL-V2 model solution, the concentration of mean turbulence kinetic energy slightly after the shock appears to have a larger spread that in the linear SST model, as indicated by the orange area in Figs. 6a and 6c.

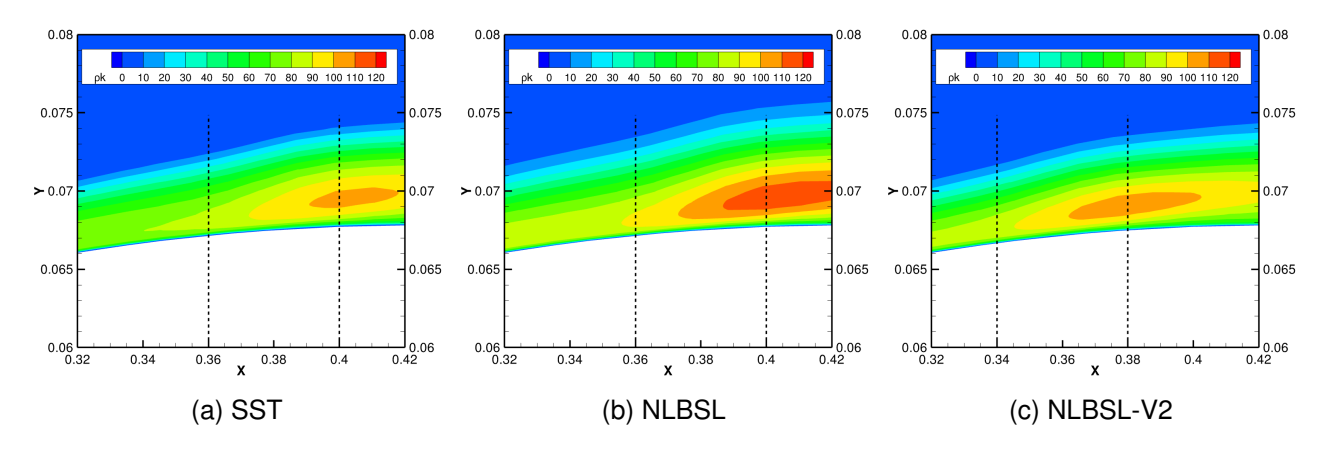


Figure 6 – Results for the  $\rho k$  field around the OAT15A airfoil. View 2 region from Fig. 4.

These results suggest that there are no characteristics in the physics of the flow solved by each turbulence model that could justify different locations of the captured shock waves. For instance, the NLBSL turbulence model compute larger  $\rho k$  levels near the shock wave and a layer of  $\rho k$  thicker than the linear SST model. However, the location of the shock wave for these two solutions is the same. Now, considering only the SST and NLBSL-V2 results, the thickness of the layer with significant production of mean turbulence kinetic energy is approximately the same for both turbulence models, Figs. 6a and 6c. Furthermore, despite the larger spread in the concentration of  $\rho k$  immediately after the shock wave computed by the NLBSL-V2 model, the levels of  $\rho k$  are similar for both solutions. Nevertheless, as discussed earlier, the solutions indicate a significant improvement in the ability of the NLBSL-V2 turbulence model to deal with transonic flows over the linear SST model.

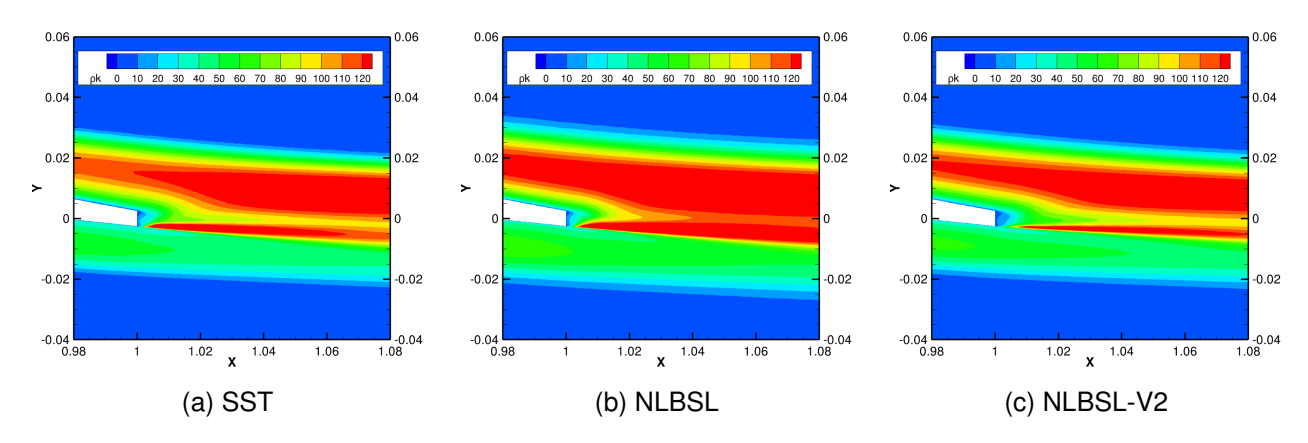


Figure 7 – Results for the  $\rho k$  field around the OAT15A airfoil. View 3 region from Fig. 4.

Figure 7 shows the region denoted as view 3 region in Fig. 4, which is the airfoil trailing edge region. This visualization shows a larger spreading of higher levels of turbulent kinetic energy for the NLBSL model solution. The maximum value of turbulent kinetic energy in the whole field is observed in the NLBSL model solution near the airfoil trailing edge, reaching a value of about 233 J/m³. The linear SST turbulence model computed the maximum value of 208 J/m³. The value achieved by the NLBSL-V2 solution is very different from the other turbulence models. For the NLBSL-V2 solution, the maximum value of  $\rho k$  in the whole field is about 150 J/m³.

Figure 8 shows the velocity profiles of the boundary layer made dimensionless by the freestream velocity. The boundary layer profile represented by the NLBSL-V2 turbulence model is in excellent agreement with the experimental data. The results presented show that the use of a more advanced turbulence model may have a very significant positive effect on the final solution for this test case.

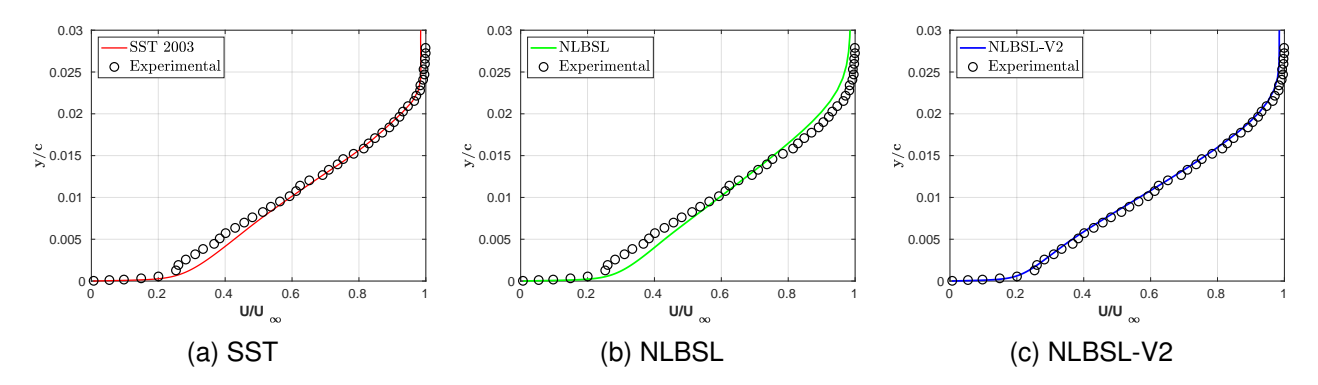


Figure 8 – Numerical and experimental boundary layers at x/c = 95% over the OAT15A airfoil.

The results presented show that the use of a more advanced turbulence model may have a very significant positive effect on the final solution. Moreover, for industrial applications, is important to obtain a good balance between accurate solutions and computational cost. Table 4 presents a relative computational cost estimate for the three turbulence models, considering the simulations of the flow over the OAT15A airfoil using the fine mesh and running 50000 iterations. There is an extra cost for the nonlinear turbulence models compared to the linear turbulence model when using the fine mesh. This is expected because nonlinear relations were included in these models. However, considering the fairly significant improvement in the results obtained with the NLBSL-V2 turbulence model, this increase in the computational cost does not seem to be really relevant for industrial applications. Of course, it is necessary to improve these turbulence models and validate them using a larger number of test cases in order to justify their inclusion in the day-to-day industrial calculations.

Table 4 – Computational cost estimates for the three turbulence models for the solution of the OAT15A airfoil flow using the fine mesh. The values correspond to the cost of 50000 iterations and are normalized by the cost of the SST 2003 solution.

Mesh Level	Nº Volumes	SST	NLBSL	NLBSL-V2
Fine	200704	1	1.12	1.13

## 4.2 Flow over McDonnell Douglas 30P30N Multi-Element Airfoil

Flows over multi-element airfoils are typical applications in the aeronautical industry. Aircraft with high cruise speeds typically use high-lift devices in order to augment both the wing area and its camber, and, hence, allow for an increase in the wing area and the wing load in low-speed regimes, such as during takeoff and landing. The main aerodynamic phenomena present in this type of flow are related to the laminar-turbulent transition, large pressure gradients, and the interaction between the boundary layers and wakes that appear between the gaps of each surface. The optimization of high-lift devices depends on accurate simulations to minimize the interactions between boundary layers and pressure gradients of the mean flow and between boundary layers and wakes.

The flow over the McDonnell Douglas 30P30N multi-element airfoil was chosen to investigate the capabilities of the EARSM turbulence models addressed here to represent the turbulent effects present in this type of flow. The results are compared with experimental data [16] and with the SST turbulence model calculations [13, 14]. The flow conditions for the simulations performed are shown in Tab. 5. Figure 9 illustrates the mesh used in this study case. Details on the high-lift surfaces can be observed

in Figs. 9a and 9c. The mesh consists of hexahedrals and the external boundary is located at 150 chords of the airfoil. The slat and flap deflections are -30 and 30 degrees, respectively.

Table 5 – Flow conditions for the 30P30N multi-element airfoil case.

$M_{\infty}$	Re	Chord [m]	$\mu_t/\mu_\infty$	$\alpha$ [deg]
0.2	$9 \times 10^6$	0.5588	3	8

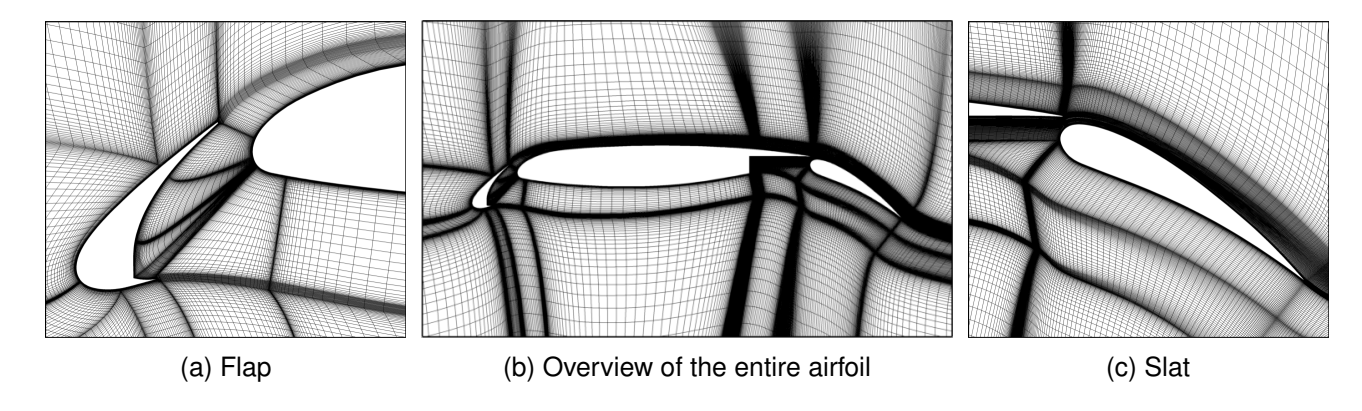


Figure 9 – Mesh over the McDonnell Douglas 30P30N multi-element airfoil with details of the high-lift devices.

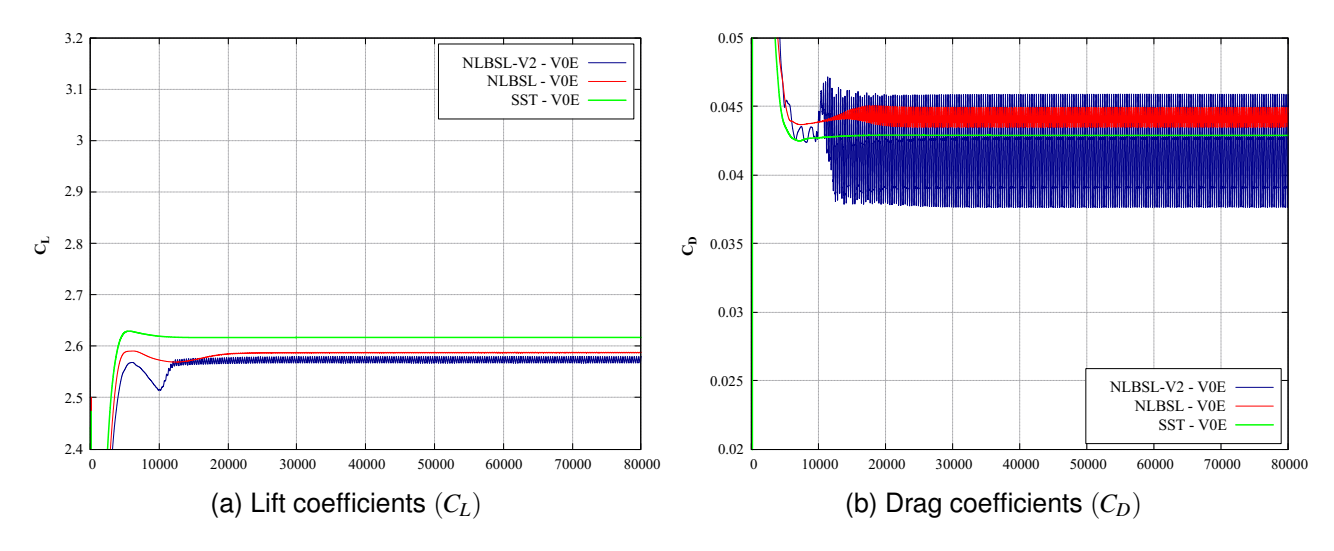


Figure 10 – Convergence history of aerodynamic coefficients,  $C_L$  and  $C_D$ , for each turbulence model.

Figure 10 shows the convergence history of aerodynamic coefficients,  $C_L$  and  $C_D$ , obtained with each turbulence model. Looking at the SST solution, which is represented by the green line, one can clearly conclude that both lift and drag coefficient values stabilize and, hence, there is convergence of the solution. The same occurs with the  $C_L$  values computed by the NLBSL turbulence model, *i.e.*, red curve. However, the drag coefficient has oscillations of about 15 counts. The solution obtained with the NLBSL-V2 model, represented by the blue curves, presents oscillations for both aerodynamic coefficients, with variations more significant in the  $C_D$  values. For the drag coefficient, such variations are of about 70 counts. Figure 11 shows the pressure coefficient distributions over the 30P30N airfoil. The results from the three turbulence models have good agreement with experimental data. For the NLBSL-V2, due to the  $C_D$  oscillations of about 70 counts, it was expected that one would observe some significant differences between this solution and the results from the other models. However, these differences are not really seen in the pressure coefficient distributions.

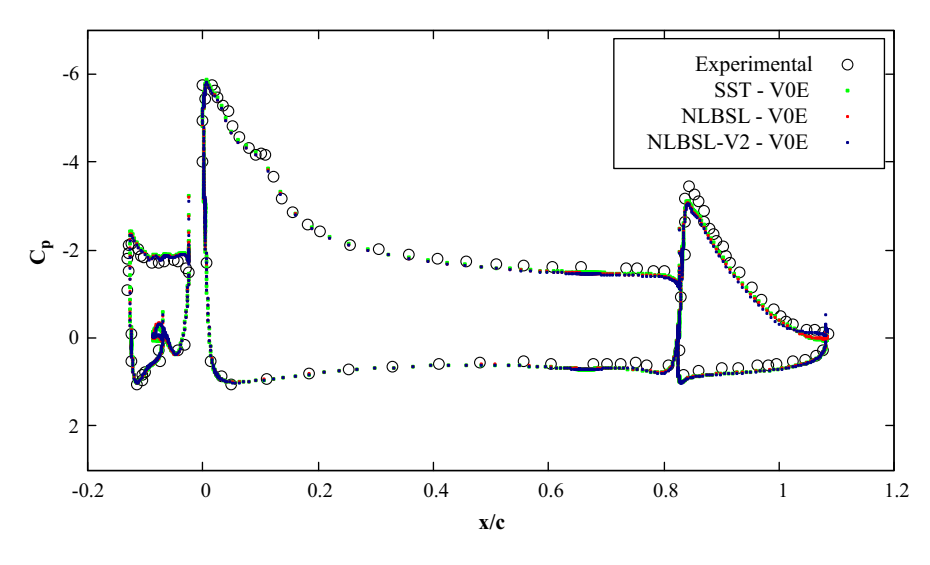


Figure 11 – Pressure coefficient distribution over the 30P30N multi-element airfoil.

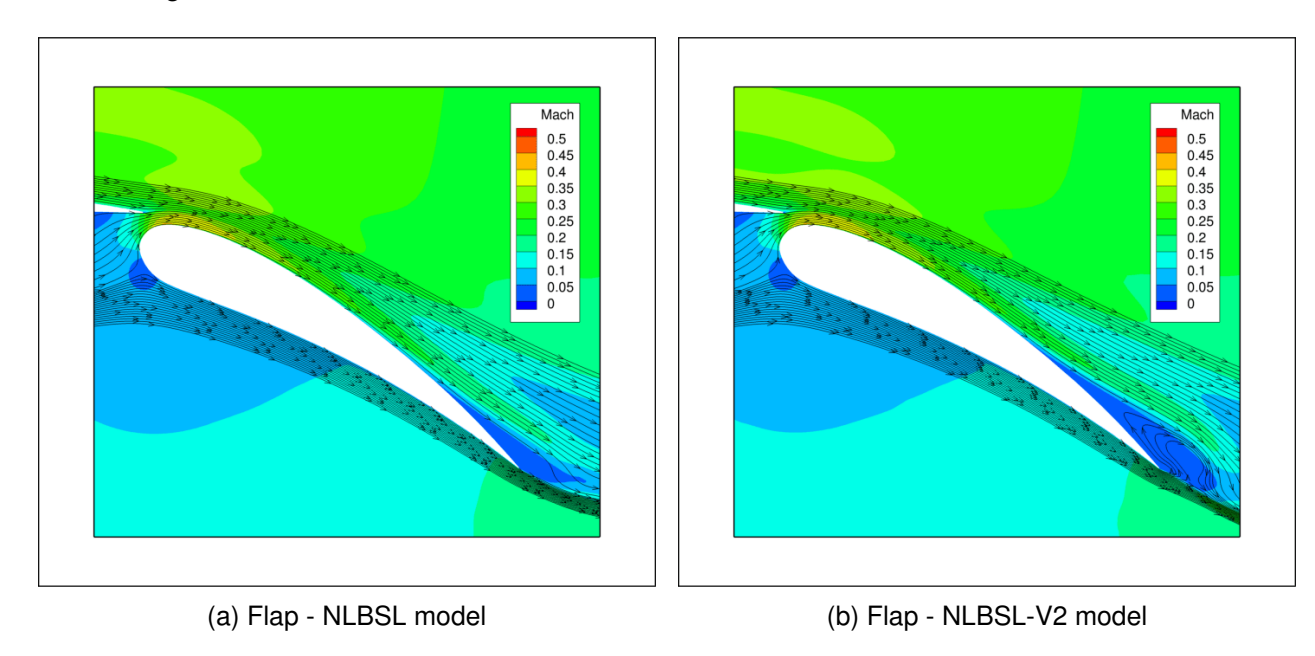


Figure 12 – Visualization of the streamlines to observe the separation phenomenon on the trailing edge of the flap.

Given these results, some investigations were made to identify the reason for the oscillations in the solutions computed with the nonlinear turbulence models. The experimental test [16] reports that there is flow separation at the trailing edge of the flap. However, it is not clear whether the separation bubble shows any type of unsteady behavior. Figure 12 shows the streamlines in the region of the flap. The NLBSL-V2 solution, Fig. 12b, computed the location of the flow separation more upstream than the NLBSL solution. However, the presence of this physical phenomenon does not seem to be sufficient to determine if this study case is an unsteady problem.

Figure 13 shows the distribution of the pressure coefficient over the flap obtained at different instants along the convergence process. This analysis has the purpose of identifying whether there are significant changes in the pressure coefficient distributions between these iterations and, thereby, it could explain the oscillations of the aerodynamic coefficients computed with the nonlinear turbulence models, especially, the large variations of the drag coefficients computed with the NLBSL-V2 model. However, for both nonlinear turbulence models, the results do not show significant differences in the pressure coefficient distributions over the flap that may be considered large enough to justify the oscillations of about 70 counts in the drag coefficient.

Given these results, one hypothesis considered was that the limiter function could lead to such vari-

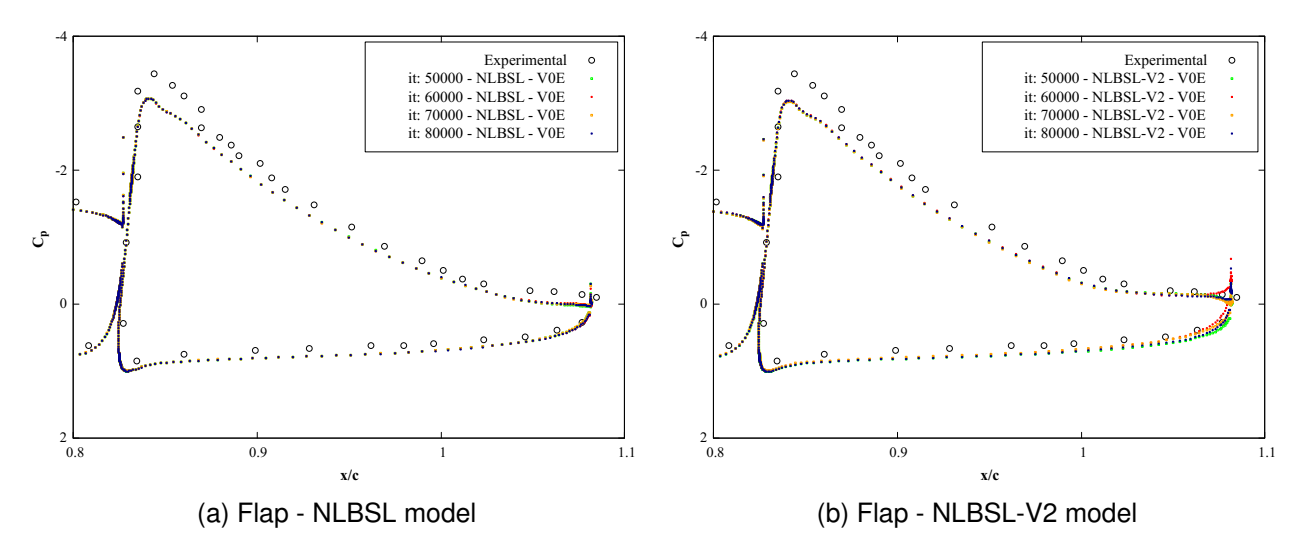


Figure 13 – Pressure coefficient distributions on the flap of the 30P30N multi-element airfoil. Results obtained at different instants along the convergence process.

ations in the solutions. To evaluate this, simulations were run freezing the limiter function at iteration 10000. It means that, after iteration 10000, the simulation will keep the function limiter value calculated at the iteration 10000 until the end of the simulation. Figure 14 shows the convergence history of the drag coefficient obtained with both nonlinear turbulence models. Green curves represent the solutions obtained with the limiter function turned on during the whole simulation and the blue curves represent the solutions obtained with the limiter function frozen at the iteration 10000. For the NLBSL results, Fig. 14a, the drag coefficient stabilizes, but, after some iterations, the oscillations return. For the NLBSL-V2 results, Fig. 14b, there is no evidence that the limiter function has any effect on the convergence of the drag coefficient.

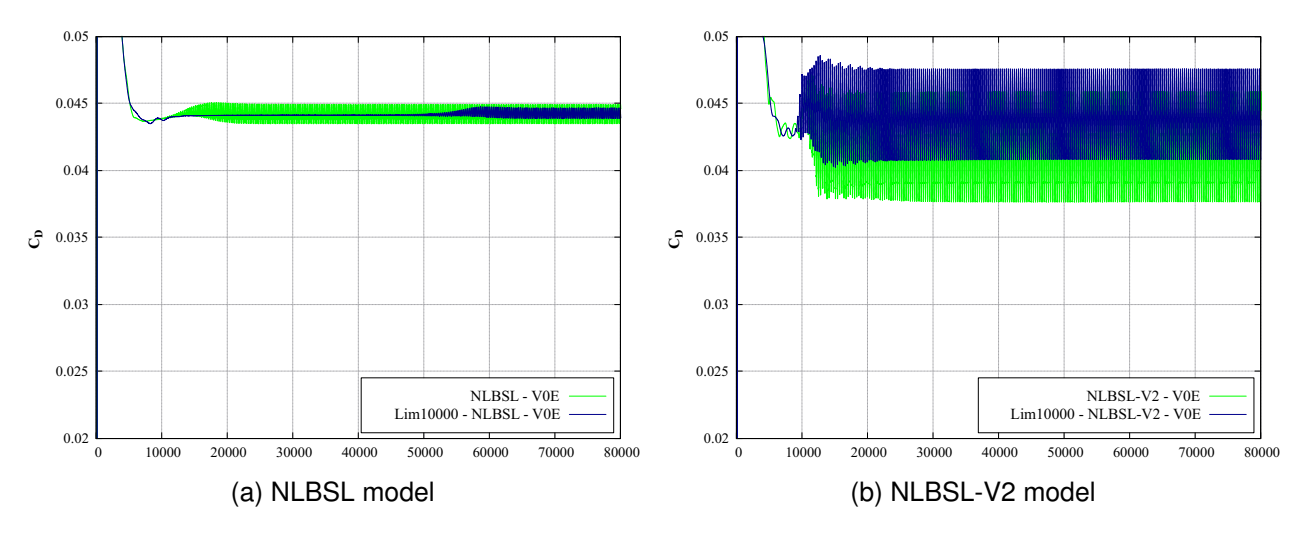


Figure 14 – Convergence history of drag coefficient computed with the nonlinear turbulence models with the limiter function frozen at the iteration 10000.

Although the anisotropic contribution of the nonlinear turbulence models could not be observed for this case, the convergence history of the aerodynamic coefficients shows that there are effects of the non-linearities present in these models. The aerodynamic coefficient results indicate that a steady-state solution is not being reached with the nonlinear turbulence models. However, the transient indicated in the variations in Fig. 10 is not a real transient, because, in order to obtain a steady-state solution, all solutions presented were computed with a constant CFL number. Such results indicate that perhaps it is not possible to achieve a formal convergence of the solution with this nonlinear turbulence model for this test case.

It should also be observed that, although a mesh refinement study has not been performed in this case, the mesh used was generated with the best industry practices. Therefore, it seems to be an appropriate mesh for the problem [17]. However, since the nonlinear turbulence models are not common in the daily industry routine, a mesh refinement is an interesting study to be performed in the future to observe if the mesh has any influence in the lack of formal convergence of the aerodynamic coefficients for this case.

#### 5. Conclusions

The present work is concerned with the use of nonlinear eddy-viscosity turbulence models in aeronautical applications with a computational cost that could be used in daily engineering applications. The results obtained so far with the nonlinear turbulence models in the present investigation are very encouraging. In the OAT15A airfoil case, the compressibility effects present in the nonlinear formulation of the NLBSL-V2 turbulence model seem to be very important for obtaining a better agreement on the shock wave position. The results also indicate that this improvement in the representation of the shock wave had a modest computational cost.

Given the results of the flow over the McDonnell Douglas 30P30N multi-element airfoil, the nonlinear turbulence models did not reach a formally converged solution for the aerodynamic coefficients. The source of the oscillations in aerodynamic coefficients has not been identified. As already indicated, it is important to fully understand the reasons for this lack of formal convergence in the future in order to complete the validation of these turbulence models. In general, it is important to emphasize that the computational cost estimates obtained for the 2-D test case of the transonic airfoil encourage the study of the nonlinear turbulence models in order to obtain more accurate representations of complex flows for industrial applications at acceptable costs.

# 6. Acknowledgments

The authors acknowledge the support for the present research provided by the computational resources from the Center for Mathematical Sciences Applied to Industry, CeMEAI, funded by Fundação de Amparo à Pesquisa do Estado de São Paulo, FAPESP, under the Research Grant No. 2013/07375-0. Further support to the second author under the same FAPESP Grant is also acknowledged. The authors also acknowledge the support for the present work through a doctoral scholarship to the first author under FAPESP Grant No. 2023/09177-2, associated to the Engineering Research Center for the Aerial Mobility of the Future, which has received the FAPESP Grant No. 2021/11258-5. The authors further acknowledge the support for the present research provided by Conselho Nacional do Desenvolvimento Científico e Tecnológico, CNPq, under the Research Grant No. 315411/2023-6. Finally, the authors are also indebted to the support provided by Coordenação de Aperfeiçoamento do Pessoal de Nível Superior, CAPES, under the Process No. 88887.799421/2022-00.

# 7. Contact Author Email Address

Thamires das Chagas Silva: th.daschagas@gmail.com. João Luiz F. Azevedo: joaoluiz.azevedo@gmail.com.

## 8. Copyright Statement

The authors confirm that they, and/or their company or organization, hold copyright on all of the original material included in this paper. The authors also confirm that they have obtained permission, from the copyright holder of any third party material included in this paper, to publish it as part of their paper. The authors confirm that they give permission, or have obtained permission from the copyright holder of this paper, for the publication and distribution of this paper as part of the ICAS proceedings or as individual off-prints from the proceedings.

## References

- [1] Duraisamy, K., Spalart, P. R., and Rumsey, C. L. Status, emerging ideas and future directions of turbulence modeling research in aeronautics. NASA TM-2017-219682, 2017.
- [2] Hellsten, A. New advanced *k*-ω turbulence model for high-lift aerodynamics. *AIAA Journal*, Vol. 43, No. 9, pp. 1857–1868, Sep. 2005.
- [3] Chagas Silva, T. *Nonlinear Eddy-Viscosity Turbulence Models for Simulations of Compressible Flows in Aeronautical Applications*. Master's Thesis, Instituto Tecnológico de Aeronáutica, São José dos Campos, SP, Brazil, 2021 (in Portuguese).
- [4] Bigarella, E. D. V. and Azevedo, J. L. F. A unified implicit CFD approach for turbulent-flow aerospace-configuration simulations. 47th AIAA Aerospace Sciences Meeting Including The New Horizons Forum and Aerospace Exposition, AIAA Paper No. 2009-1473, Orlando, FL, Jan. 2009.
- [5] Roe, P. L. Approximate Riemann solvers, parameter vectors, and difference schemes. *Journal of Computational Physics*, Vol. 43, pp. 357–372, 1981.
- [6] van Leer, B. Towards the ultimate conservative difference scheme. V. A second-order sequel to Godunov's method. *Journal of Computational Physics*, Vol. 32, No. 1, pp. 101-136, Jul. 1979.
- [7] Bigarella, E. D. V. and Azevedo, J. L. F. A study of convective flux computation schemes for aerodynamic flows. 43rd AIAA Aerospace Sciences Meeting and Exhibit, AIAA Paper No. 2005-633, Reno, NV, Jan. 2005.
- [8] Blazek, J. *Computational fluid dynamics: principles and applications*. Elsevier Science Ltd, Oxford, 3 edition, 2015.
- [9] Cary, A. W., Dorgan, A. J., and Mani, M. Towards accurate flow predictions using unstructured meshes. 19th AIAA Computational Fluid Dynamics, AIAA Paper No. 2009-3650, San Antonio, TX, Jun. 2009.
- [10] Oliveira, F. B. and Azevedo, J. L. F. Assessment of interface gradient reconstruction techniques for finite volume methods in aerospace applications. *AIAA AVIATION 2023 Forum*, AIAA Paper No. 2023-3241, San Diego, CA and Online, Jun. 2023.
- [11] Wallin, S. and Johansson, A. V. An explicit algebraic Reynolds stress model for incompressible and compressible turbulent flows. *Journal of Fluid Mechanics*, Vol. 403, pp. 89–132, Jan. 2000.
- [12] Menter, F. R., Kuntz, M., and Langtry, R. B. Ten years of industrial experience with the SST turbulence model. 4th International Symposium on Turbulence, Heat and Mass Transfer, pages 625–632, Eds.: Hanjalić, K., Nagano, Y. and Tummers, M., Begell House Inc, Antalya, Turkey, Oct. 2003.
- [13] Carvalho, L. M. M. O., da Silva, R. G., and Azevedo, J. L. F. Numerical effects of flux calculation schemes for unstructured grid turbulent flow simulations. *AIAA Aviation 2019 Forum*, AIAA Paper No. 2019-2924, Dallas, TX, Jun. 2019.
- [14] Rumsey, C. Turbulence modeling resource web page. https://turbmodels.larc.nasa.gov/, Last access: Jun. 2024.
- [15] Roddle, A. M. and Archambaud, J. P. OAT15A airfoil data. In: *A Selection of Experimental Test Cases for the Validation of CFD Codes*, NATO AGARD, No. AGARD-AR-303, Aug. 1994.
- [16] Chin, V. D., Peters, D. W., Spaid, F. W., and McGhee, R. J. Flowfield measurements about a multi-element airfoil at high Reynolds numbers. *Proceedings of the 24th AIAA Fluid Dynamics Conference*, AIAA Paper No. 93-3137, Orlando, FL, Jul. 1993.

[17] Carvalho, L. M. M. O., da Silva, R. G., and Azevedo, J. L. F. A contribution to the simulation of transitional flows over aerospace configurations. *Proceedings of the 32nd Congress of the International Council of the Aeronautical Sciences*, ICAS Paper No. 2020-0734, Shanghai, China, Sep. 2021.